vehicles

MDPI

Article

Optimization, Design, and Manufacturing of New Steel-FRP Automotive Fuel Cell Medium Pressure Plate Using Compression Molding

Sharath Christy Anand, Florian Mielke, Daniel Heidrich and Xiangfan Fang *

Institute of Automotive Lightweight Design, University of Siegen, 57076 Siegen, Germany; sharath.anand@uni-siegen.de (S.C.A.); florian.mielke@uni-siegen.de (F.M.)
* Correspondence: xiangfan.fang@uni-siegen.de

Abstract: In this work, a new plastic-intensive medium-pressure plate (MPP), which is part of a fuel-cell system, has been developed together with a steel plate meeting all mechanical and chemical requirements. This newly developed MPP had to achieve the objective of saving weight and package space. The use of compression molding as a manufacturing technique facilitated the use of glass mat thermoplastics (GMT) which has higher E-modules and strength compared to most of the injection molded materials. A steel plate was placed as an insert to help achieve the stiffness requirements. For the development, the existing MPP was benchmarked for its structural capabilities and its underlying functional features. Four different FRP materials were investigated in terms of their chemical and mechanical properties. PP-GMT material, which has both high mechanical performance and resistance against chemicals in the fuel cell fluid, had been chosen. Using the properties of the chosen PP-GMT material, topology optimization was carried out based on the quasi-static load case and manufacturing constraints, which gave a load-conforming rib structure. The obtained rib structure was utilized to develop the final MPP with adherence to the functional requirements of MPP. The developed plastic-intensive MPP exhibits a 3-in-1 component feature with a 55% reduction in package space and an 8% weight reduction. The MPP was virtually analyzed for its mechanical strength and compared with the existing benchmark values. Finally, a press tool was conceptualized and manufactured to fabricate the new plastic-intensive MPP, which was tested in a rig and validated in the FE model.

Keywords: fuel cell; medium-pressure plate; structural optimization; compression molding; GMT; package saving; light weight

check for updates

Citation: Anand, S.C.; Mielke, F.; Heidrich, D.; Fang, X. Optimization, Design, and Manufacturing of New Steel-FRP Automotive Fuel Cell Medium Pressure Plate Using Compression Molding. *Vehicles* **2024**, *6*, 850–873. https://doi.org/10.3390/vehicles6020041

Academic Editors: Ralf Stetter, Udo Pulm and Markus Till

Received: 11 April 2024
Revised: 18 May 2024
Accepted: 23 May 2024
Published: 25 May 2024

Copyright: © 2024 by the authors. Licensee MDPI, Basel, Switzerland. This article is an open access article distributed under the terms and conditions of the Creative Commons Attribution (CC BY) license (https://creativecommons.org/licenses/by/4.0/).

1. Introduction and State of the Art

A globally accepted fact in the current decade is the effect of global warming on climatic changes, which is mainly caused by CO_2 emissions. It was published by Lamb et al. [1] that in 2018, the automotive sector contributed 14% to the overall global CO_2 emissions. This, in turn, creates an emphasis on the necessity to reduce the emissions of vehicles, which translates to a steep rise in the need for vehicles powered with green energy where the carbon emissions are zero. Therefore, the sales of battery electric vehicles (BEVs) have increased in the past decade [2], and projected figures show that the market share of electric vehicles (EV) will be more than 80% in a few decades. Although extensive research has been invested in increasing the energy density of lithium-ion batteries, currently, the energy storage ability still does not meet the demands of many customers. Many consumers consider the charging time of 20 to 30 min for a 200 to 300 km driving range to be still too long [3].

This is where a polymer electrolytic fuel cell (PEMFC) can help plug the gap since the charging time is within 5 min for a driving range of more than 500 km, which is comparable to gasoline-powered vehicles [4–6]. The advantage of a continuous power supply with

the availability of PEMFC hydrogen fuel has made it a strong candidate for powering automobiles. Over the years, smaller power-demand vehicles (50–250 KW) powered by fuel cells have been on the automotive market [7]. Fuel cell vehicles can exhibit a high range with smaller increases in the weight of the vehicles in comparison to BEVs [8].

In Figure 1, a simplified schematic sketch of PEMFC, which consists of multiple cells, is shown. Each cell is an assembly of two bipolar plates, bipolar anode and bipolar cathode, which sandwich the membrane electrode assembly. A current collector is placed at the end of these cells in order to collect the electricity. Eventually, the medium-pressure plate (MPP) holds all the single cells inside the stack house. The membrane electrode assembly consists of a proton exchange membrane, catalyst layers and gas diffusion layers. The membrane transports hydrogen protons from the anode to the cathode. The catalyst layer is where the electrochemical reaction takes place, which controls the rate of the reaction based on the necessity of power. The gas diffusion layer is effectively the electrical conductor that transports the electrons to and from the catalyst layer [9]. The reactant gases, hydrogen and oxygen, are supplied to the anode and cathode via the flow ducts of bipolar plates. Electric current is generated by the electrochemical reactions, accompanied by heat development. Therefore, the bipolar plates must be cooled by coolant, for which inlet and outlet ducts must be introduced.

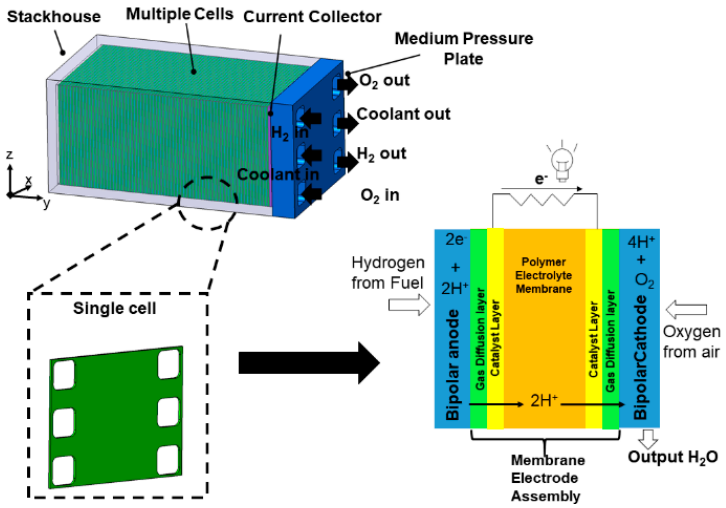


Figure 1. Schematic representation of PEM fuel cell and its working principle.

Lightweight design is an important factor in reducing the fuel consumption of vehicles using combustion engines and/or increasing the driving range of electric vehicles. Various forms of research have been carried out to reduce the weight and redesign the bipolar plates [10–13] to improve the efficiency of PEM fuel cells. Liu et al. performed a 2D shape optimization on the endplate of fuel cells, converted this optimized shape into a 3D structure, and performed FE analysis to check its structural rigidity [14]. A structural study to evaluate the contact pressure of end plates based on bolting strategies was researched by Dey et al. [15].

The body structures of vehicles must often be strongly modified if PEMFCs are to be used as power sources due to their spatial requirements, which results in higher development and manufacturing costs. Package saving in the fuel cell may thus contribute to a faster transition from combustion engines to fuel-cell electric vehicles. Package space saving should ideally be realized in components meant for structural rigidity or support, like Fuel cell housing or the medium-pressure plate, which is the topic of this work. The saved package can be used to increase the number of fuel cells, which helps increase the overall power, and the power output of the stack can be increased [16,17].

1.1. Medium-Pressure Plate

The MPP, commonly manufactured by aluminium casting or steel plate, functions as a manifold through which hydrogen, air and coolant are supplied and regulated to the PEMFC Stack [6]. As the name suggests, it also ensures a large contact force is applied to the bipolar plates, on the stack side, within the stackhouse. Bolted at different locations to the stackhouse, it also needs to guarantee an impervious working condition of the fuel cell stack [15]. The last bipolar plate is in contact with a titanium plate, which acts as the current collector.

The PEMFC stack can be subjected to various loading and stress conditions based on utility in real-time scenarios, where the PEMFC should have a >40,000 h static work lifetime and >5000 h automotive application lifetime [18]. Yan et al. have also reported that the performance of PEMFC is also influenced by temperature and humidity, which affect the charge transfer resistance of the stack [19]. These stress conditions increase the emphasis on the material characteristics of the fuel cell system.

The reference MPP of this work is made of aluminium casting with a layer of glass fibre-reinforced polyphenylsulfide (PPS) material with 30% glass fibre reinforcement per weight, injection molded on the cast aluminium. The FRP layer here acts as an insulation between the aluminium and current collector [20].

A PEM fuel cell system is typically operated between 65 °C up to 125 °C [21] using perfluorosulfonic acid HCOO-CF(CF_3)-O-CF_2CF_2-SO_3H (PFSA) polymers such as Nafion as membranes for their superior conductive and chemical properties [22]. PFSA can also be shortly represented as R_f-CF_2COOH, where R_f represents the non-reactive part of the Nafion molecule. The chemical requirement of MPP is that it should exhibit high resistance to moisture, hydrogen, and acid mediums as there is direct contact with these mediums. Chemical degradation of PFSA is a major issue in PEMFCs. This degradation is due to the dissociation of hydrogen peroxide molecular bonds, which is due to the presence of metal ions like Fe Cu through the corrosion of cell or stack materials [8].

$$\text{Metal ions}\left(M^{(Z+1)}\right) + H_2O_2 \rightarrow M^z + +HO^{\cdot} + H^+ \quad (1)$$

Radical Hydrogen ions get washed out due to the dissociation of hydrogen peroxide (H_2O_2). Oxidative hydroxyl ($HO^{\cdot}$) and hydroperoxyl ($HOO^{\cdot}$) are also produced due to the decomposition of hydrogen peroxide. The oxidative hydroxyl groups react with the carboxylic acid group (–COOH), as shown in Equations (2) and (3), giving rise to a degrading effect on the PEMFC membrane. This phenomenon is termed an "unzipping mechanism" [8,23].

$$R_f - CF_2COOH + HO^{\cdot} \rightarrow R_f - CF_2 + CO_2 + H_2O \quad (2)$$

$$R_f - CF_2 + HO^{\cdot} \rightarrow R_f - CF_2OH \rightarrow R_f - COF + HF \quad (3)$$

$$R_f - COF + H_2O \rightarrow R_f - COOH + HF \quad (4)$$

The hydrogen ion attacks the washed-off fluorine atoms from PFSA and forms a hydrogen fluoride (HF) acidic medium, which is termed free radical attack. Hydrogen fluoride is particularly aggressive towards the FRP materials used to create the insulation layer on MPP, including the glass fibres. The reaction of hydrogen fluoride with glass fibres can subsequently increase the pH values within the fuel cell system, which can lead to detrimental effects. Due to the acidic medium, it was imperative that the FRP should be free of any cracks as the acidic medium will seep into the microstructure of FRP and rapidly degrade it.

Currently, many polymers are used in the manufacturing of PEMFCs. Gaskets within the fuel cell systems may comprise various polymers such as polyester, polyimide, polyethylene naphthalate, and polyethylene terephthalate. Gas diffusion layers are made using porous substrate comprising of fluorinated polymers such as polytetrafluoroethylene

(PTFE) and fluorinated ethylene propylene (FEP) [24]. Due to its ability to transport gases or components of dissolved liquids, a widely used polymer in PEMFC is PPS-based FRP material [25].

On the functional side, the MPP has six through holes for various fluid mediums to pass in and out of the stack. For the development of the new plastic-intensive MPP, it was important to capture the entry and exit cross sections of these through holes as it enables a smooth transition of the newly developed MPP into the existing fuel cell systems. However, there were few adaptions made in the geometrical boundary conditions of these through holes, which will be discussed in the following chapter.

On the other side of the medium-pressure plate is the medium interface unit (MIU), which is a combination of MIU housing (see Figure 2) onto which different pumps, sensors and piping systems are bolted that regulate the flow of different fluid medium in and out of the fuel cell stack [26]. Although not prescribed with stiffness requirements, the MIU housing needs to be stiff enough for the various neighbouring components to be bolted upon.

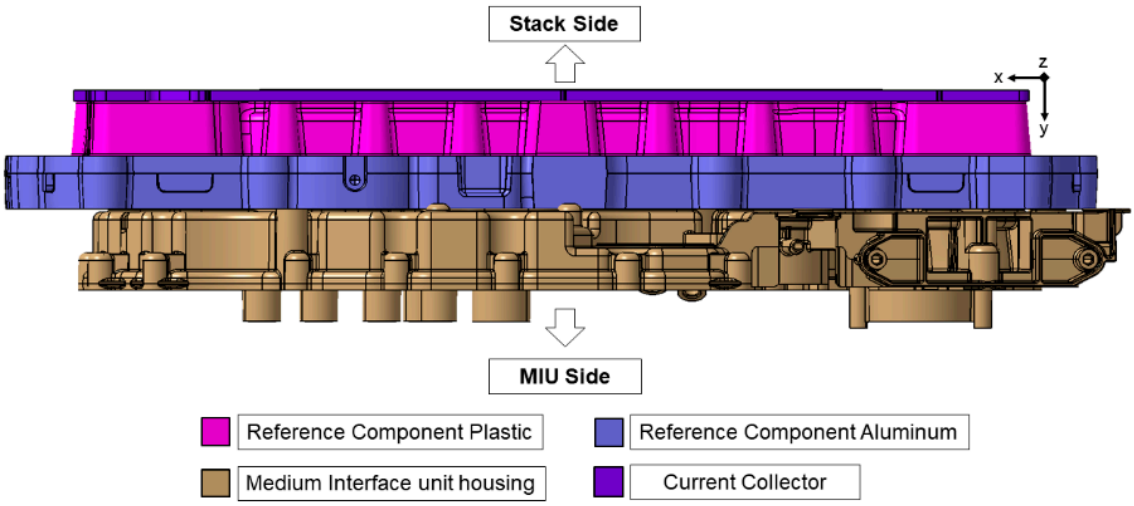


Figure 2. Reference medium pressure plate with medium interface unit.

In this work, the MIU housing will be integrated into the MPP to achieve component integration. Hence, the space occupied by the current MIU housing will be considered for the FRP design space for topology optimization. Due to the larger overall thickness of the MIU housing, it should also be able to carry loads to achieve an improved mechanical property of the entire MDP. Therefore, both material selection and the geometric design of MIU housing are important. Since FRP components are predominantly manufactured with ribs for reinforcements and functionality, the design and placement of these ribs need to be conducted to withstand loads. A topology optimization is one way to predict the rib structure for a given load case.

1.2. Topology Optimization

Topology optimization is basically optimization where a pre-defined design space is created, which is then applied with geometrical and manufacturing constraints based on the functionality of the resulting component. During a topology optimization, an FE simulation is carried out over different iterations along with a design objective. The optimization variables are continuously adjusted over the different iterations until iterative tolerances are achieved [27]. On reaching convergence, the final result is normally a rib geometry with the best possible scatter of material in terms of load-bearing capacity.

The methodology behind topology optimization is a density-based approach incorporating the solid isotropic material with the penalization method (SIMP). In this method, the material density of each element (ρ) of the design space is set as a design variable and

varied continuously between 0 and 1 [28]. Here, the densities 0 and 1 correspond to the condition of void or presence of an element, respectively. As the optimization tends to reach convergence, the penalty factor (p) eliminates elements with intermediate densities. In Equation (5) $\underset{\sim}{\boldsymbol{K}}$ is the penalized stiffness matrix, and **K** is the real stiffness matrix [15,28].

$$\underset{\sim}{\boldsymbol{K}}(\rho) = \rho^{P}\mathbf{K} \tag{5}$$

An optimization with an overall goal of attaining a rib structure with a fraction of mass removal from the design space allowed is normally set with a compliance minimization criterion. Compliance, as given in Equation (6), is defined as the flexibility of the component and the inverse of stiffness. This means a structure's global compliance (C) is the addition of the strain energies of the elements of the design space. Reduction of the global compliance maximizes the global stiffness as given in Equation (7), where e are elements in the design space [29].

$$C = \frac{1}{2}u^{T}\mathbf{K}u \tag{6}$$

$$\min C(\{\rho\}) = \sum_{e=1}^{N}(\rho)\left[u^{T}\right][K][u] \tag{7}$$

The culmination of methodology with optimization constraints and objectives is set into an iterative phase, wherein different rib structures are built based on the goal, and eventually, a raw rib structure is formed which is in compliance with the given load case and at the same time adhering to the applied manufacturing constraints.

1.3. Compression Molding

A well-known manufacturing technique used in the automobile industry to produce Fibre-reinforced plastic parts is injection molding. During the injection phase, fibre lengths reduce through shearing of the rotating screw and typically have lengths between 400–700 microns. This fibre length is further reduced through the injection nozzles. Increasing the fibre length can significantly increase mechanical properties, especially strength and energy absorption [30,31]. The property that increases fibre length gives better mechanical properties and paves the way for compression molding.

Compression molding employs similar machines to produce the raw FRP compound with a given percentage of fibre content. As the name suggests, in compression molding, a vertical press machine is used to press the parts into shape rather than a horizontal machine used in injection molding [32]. A schematic representation of compression molding is shown in Figure 3. Due to the delayed introduction of fibres in the extruder, fibre damages are mitigated. Here, the molten FRP taken from the extruder is placed in the open mold cavity and pressed into the cavity contour through press force, where a fibre length of up to 25 mm could be achieved in the final part [33].

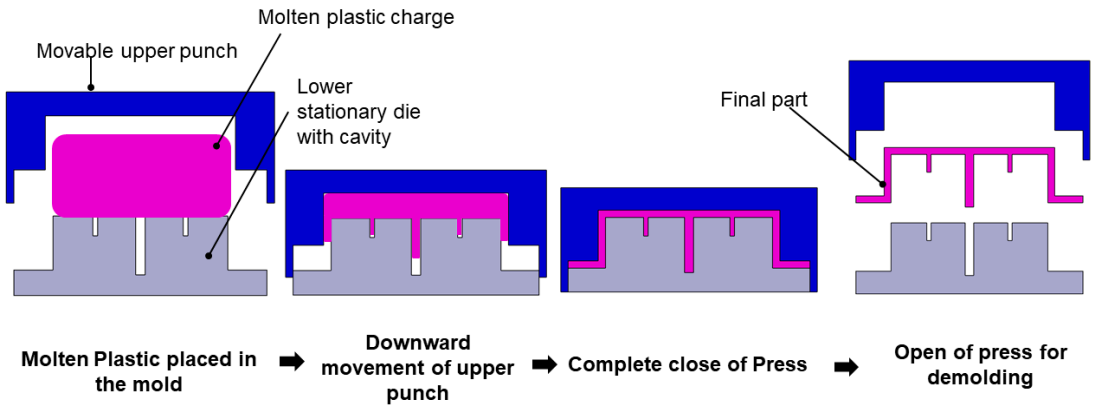


Figure 3. Compression molding schematic.

The advantage of achieving high fibre lengths in parts makes compression molding a useful manufacturing method that will be used for the manufacturing technique for this work.

1.4. Target of the Work

Liu. B et al. [14] have presented research on the virtual shape optimization of pressure plates by studying the shape-related parameters that influence the final design of pressure plates. Similarly, in the works of Liu [14], Lin. P et al. [13] and Dey. T et al. [15] have also presented a virtual design solution for pressure plate designs through various optimization methodologies. These studies end with only the virtual design and development of different pressure plates. This opens the avenue for the authors of this paper to not only virtually develop a new design concept for the medium-pressure plate but also extend this development chain into the suitable material selection, manufacturing the new concept and performing mechanical tests.

Furthermore, the benchmarked fuel cell stack and the corresponding MPP shown in Figure 2 are foreseen for Fuel Cell Units of bigger passenger vehicles like sport utility vehicles (SUV). Therefore, the target of the current work is to develop a new steel plus plastic-intensive medium-pressure plate that can save package space and reduce weight. In order to achieve this goal, another kind of FRP material must be used instead of standard PPS with higher strength and Young's modulus. The idea is to use the FRP not only as an insulator but also as a structural component of the pressure plate. Since compression molding enables a higher strength of FRP, this technique should be used, and both material properties and the manufacturing process for the pressure plate should be investigated using this process. In addition, the chemical resistance of the FRP materials must be measured for the final material selection.

The new plastic-intensive MPP should also enable a high component integration besides high strength and rigidity, which should be obtained by using topology optimization. The new space-saving MPP should enable the usage of fuel cells in smaller vehicles instead of larger SUVs.

2. Conceptualization and Process Framework

In order to achieve the above-mentioned goals, certain adaptations to the installation space had to be taken into consideration. These adaptations were decisions made in close cooperation with the OEMs with a futuristic view of the fuel cell system requirements.

The basic idea of the new plastic-intensive MPP is to integrate the MIU housing into the MPP and use FRP material with enhanced E-modules and strength compared to the state-of-the-art. The functionality of MIUs should be combined with their stiffness and strength so that the MPP can be designed with reduced thickness. In addition, since the specific bending stiffness of aluminium is not higher than that of steel, a steel plate should be used to reduce the thickness of MPP by more than 50%.

As shown in Figure 4, the overhang of the MIU housing in the Z-direction and a few sensor hole features were neglected to reduce the complexity of manufacturing the reference medium-pressure plate (Figure 4a) after discussion with the OEM. Opening for the coolant out has been moved to the new position, as shown in (Figure 4b). The cavity for the cooling channel, depicted in orange in Figure 4b, behind the current collector, was deemed unnecessary and thus removed. In addition, it was decided that the bolting locations for various module units had to be recreated as in the reference MIU housing. Gasket lines, where necessary, were also recreated exactly as in the reference MIU housing to facilitate the ease of assembly integration and the use of existing parts.

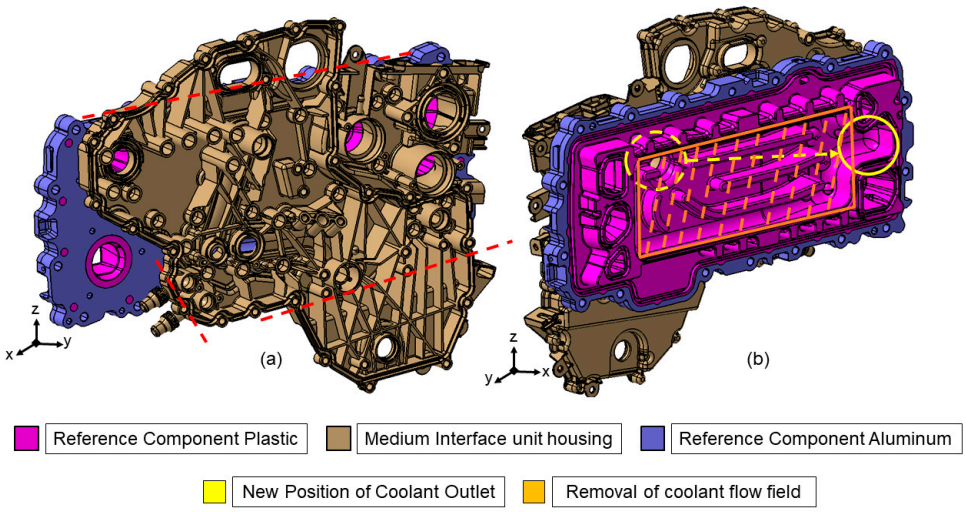


Figure 4. (**a**) Adaptations in the existing medium interface unit housing and (**b**) adaptations in the reference pressure plate.

Once the conceptual adaptations were fixed, a methodology was developed to achieve the goal of this work. The methodology takes into account all the key constraints and boundary conditions like stiffness and function requirements. As shown in Figure 5, the process starts with the reference phase, where stiffness performances of the existing MPP are benchmarked through FE Simulation of the critical load case. Additionally, the package space required for the existing MPP and MIU was taken into account.

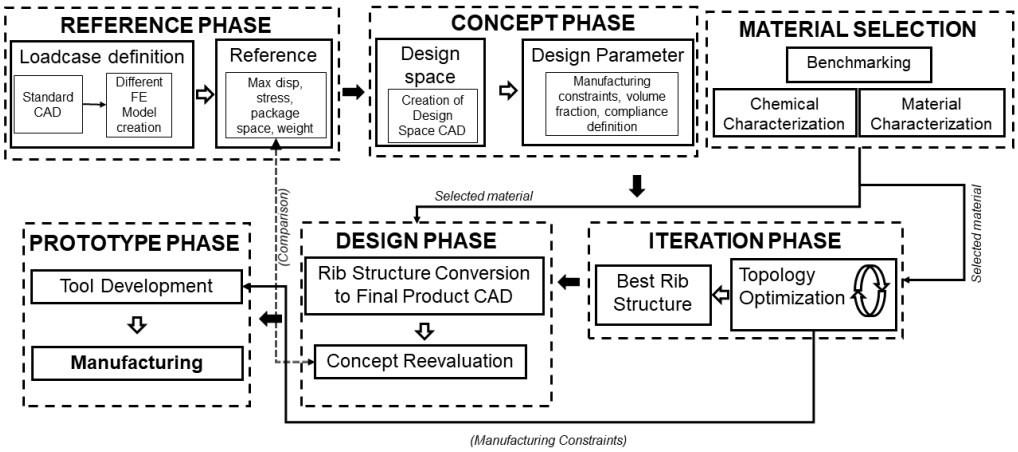


Figure 5. Process framework.

This was followed by the concept phase, where the design space for the topology optimization was first created, and further conditions, such as manufacturing and geometrical conditions, such as rib height, rib thickness, and draw directions, were defined. These conditions eventually determine the outcome of the rib structure over an iterative FE analysis coupled with optimization. In the material selection and characterization phase, suitable materials were chosen and characterized for their strength and chemical behaviour. The obtained rib structure is taken into the design phase, where it is built around and converted into the final plastic-intensive MPP in a CAD environment, capturing important functional aspects like sealing lines or neighbouring component bolt locations. Here, within the sub-phase of concept revaluation, the final MPP is subjected to the critical load case to see if it meets the expected structural requirements.

For the topology optimization and the final FE calculation of the MPP performance, the properties of the FRP must be determined as FEM material input data. Several FRP materials were thus analysed in comparison to the reference materials.

Once the final CAD was approved, the concepts for tool design for the manufacturing were developed, and the press tool was developed. Here, manufacturing constraints used during the topology optimizations were fed as input for the press tool development. The new plastic-intensive medium-pressure plate was manufactured with the press tool manufactured and taken into commission.

3. Materials

3.1. Material Characterization

As mentioned in Section 1.3, the newly developed MPP in this work will incorporate a higher percentage of FRP material in its construction and use steel plates for stiffness and strength purposes. As mentioned in Section 1, the fuel cell stack works at extreme conditions of temperature and working mediums, which raises the requirements of the materials being used for the manufacturing of MPP. The existing reference MPP has an injection molded short glass fibre-reinforced PPS layer with a 30% fibre content. Within the scope of this work, four different materials described in Table 1 were investigated and characterized. Compared to the reference PPS material, polypropylene (PP) and polyamide (PA) are standard thermoplastic materials and very much cheaper. It could be used to reduce the cost and increase the performance of MPP if their properties are acceptable or even better than the PPS reference.

Table 1. Materials selected for characterization.

Material Name	Sample Norm and Manufacturing Technique	Material Description
PP-X121 F42	DIN EN ISO 527-4 Type 2, Rectangular sample—water-jet-machined	Polypropylene-based glass mat thermoplastic with 42% glass fibre content, including 2 layers of woven fibres
PP-X103 F61	DIN EN ISO 527-4 Type 2, Rectangular sample—water-jet-machined	Polypropylene-based glass mat thermoplastic with 61% glass fibre content, including 2 layers of woven fibres
PA66-GF50	DIN EN ISO 527-2 Type 5A, shoulder sample—water-jet-machined	Polyamide-based thermoplastic with 50% short glass fibre
Reference PPS GF30	DIN EN ISO 527-2 Type 5A, shoulder sample—direct-injection molded	30% short glass fibre content

The materials were analysed in terms of their chemical and mechanical behaviours. The chemical behaviour includes mainly the resistance of the material against the acid medium, and the mechanical properties were measured by quasi-static tensile tests. The same samples were used for both analyses.

Depending on the fibre length of the material, the sample norm was selected. The material architecture of PP-X121 F42 and PP-X103 F61, delivered by Mitsubishi Chemical Advanced Materials, consists of layers of woven fabrics and chopped glass fibres of length 50 mm. In order to avoid damage to the long glass fibres of the PP-based FRPs, rectangular samples of standard DIN EN ISO 527-4 Type 2 were cut using water jet machining. The PA66 50% glass fibre material was manufactured as flat plates using injection molding from which DIN EN ISO 527-2 Type 5A samples were taken out using water jet machining. The Reference PPS material with 30% short glass fibre was directly manufactured as DIN EN ISO 527-2 Type 5A shoulder samples using injection molding.

A major difference here was that the rectangular samples of PP-based materials and the shoulder samples of PA66-based materials had open fibre ends on the waterjet machined

edges; however, the injected molded shoulder samples had an injection polymer skin, which acts as a protection layer for the fibres.

For chemical characterization, no common standard exists. Therefore, in this work, the authors proposed the following chemical solutes and testing procedures in cooperation with OEM partners. Firstly, a solution with a mixture of distilled water and concentrated sulphuric acid (H_2SO_4) was prepared until an acidity level or pH level of 3 was 3 reached. To this mixture, 30 mg of Sodium Fluoride (NaF) salt was added per litre. This solution was termed product replacement water and recreates the worst-case working environment scenario in a PEMFC. The addition of NaF salt releases sulphate ions (SO^{4-}), sulphite ions (SO^{3-}), hydrogen sulphate ions (HSO^{4-}), and hydrogen fluoride (HF) acid is also produced.

Three samples from each material in Table 1 were placed inside a neutral, inert container filled with the fuel cell product replacement water at 95 °C. After a period of 720 h (1 month), the pH level of the product replacement water from each sample container was measured using a pH level detector. Here, an increase in pH level means an increase in acidity level, which can have detrimental effects on the fuel cell system. In addition to this, the samples were weighed before and after the immersion process to check the level of water absorption by the samples. High levels of water absorption are bad for electrical isolation, which is one of the major responsibilities of the layer of plastic on the MPP [6].

It can be seen from Table 2 that the pH value of the water rose less for the reference PPS-based FRP material than for the other materials. The reason can be found in the sample preparation and material composition. As can be seen in Table 1, the reference PPS material has less glass fibre content and no open edges since it was directly injection moulded, whereas the other three materials have higher glass fibre content with open edges due to the water jet cutting of the sample. It can be seen that the product water taken from the PP-based materials container has a lower pH value than that of the PA-based materials.

Table 2. pH values, conductivity, and water absorption of the selected materials.

Material	Fibre Orientation	pH Value	Conductivity (µS/cm)	Sample Weight before Immersion (g)	Sample Weight after Immersion Period (g)	Difference (g)	Difference (%)
Product replacement water	-	3	414	-	-	-	-
PP-X121 F42	0°	6.72	266	19.497	19.636	0.139	0.71
	90°	6.76	271	19.412	19.511	0.099	0.51
PP-X103 F61	0°	6.73	257	21.077	21.305	0.229	1.09
	90°	6.52	261	22.098	22.240	0.142	0.64
PA66-GF50		7.25	328	6.122	6.272	0.150	2.45
Reference FRP PPS GF 30		5.49	210	9.877	9.940	0.063	0.64

Considering the water absorption of the different FRP materials, the change in the sample weight shows that the PP-based materials have absorbed less water than the PA-based FRP materials. The values of PP-based materials are quite comparable to those of the reference PPS material.

Furthermore, a second step of chemical characterization was carried out. The chemical characterization was conducted by an Inductively Coupled Plasma Optical Emission Spectroscopy method (ICP-OES) using an Arcos-2 ICP-OES analyser apparatus from Spectro Analytical Instruments, with a micro-mist cross-flow nebulizer. Argon gas was used as a plasma gas. As operational parameters, 1.4 kW plasma power with 30 RPM pump speed

and a coolant flow rate of 13 L/min was used. ICP-OES is an analysis technique used to measure the element content in a sample following the principle that ions have the ability to absorb energy and reach excited states, which eventually release light at a certain wavelength [34]. ICP-OES analysis was carried out by taking 5 mL of product water from the stored sample containers after a period of 720 h to determine the washed-out elemental composition.

Table 3 shows the concentration of glass fibre components in product replacement water measured using ICP-OES analyses. Considering the reference PPS material as the benchmark values, the PA66- and PP-based FRP materials were evaluated. PP-based materials had comparable or lesser leaching content of Al, B, Li and Mg elements when compared to the reference PPS material; however, Ca, K and Na have leached out more. A comparison between the PA- and PP-based materials clearly shows that except for Si and Na, all the other elements had leached out at higher quantities by the PA-based materials.

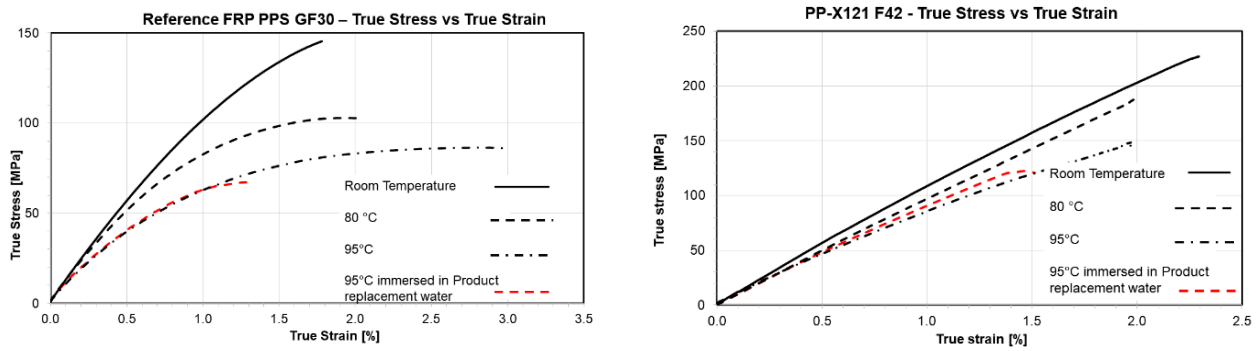
Table 3. Concentration of glass fibre components in product water.

Material	Fibre Orientation	Al [mg/L]	B [mg/L]	Ca [mg/L]	K [mg/L]	Li [mg/L]	Mg [mg/L]	Si [mg/L]	Na [mg/L]	Sr [mg/L]
Product water	-			-	0.30	-	-		15.68	
PP-X121 F42	0°	0.63	0.47	24.12	2.26	0.03	-	40.73	20.42	0.04
	90°	1.16	0.28	26.49	2.71	0.05	1.17	41.77	20.33	0.04
PP-X103 F61	0°	1.29	1.37	27.22	3.74	0.04	1.66	40.78	19.70	0.08
	90°	0.58	1.57	24.02	3.95	0.04		37.82	20.62	0.08
PA66-GF50		2.26	2.55	21.08	7.98	0.05	1.54	90.98	17.90	0.25
Reference FRP PPS GF 30		1.37	1.70	21.20	0.58	0.04	1.58	32.53	17.40	0.06

The above two material characterization studies have shown that PA-based materials show large differences in pH value, conductivity, and water absorption rates, which is not desirable for the working conditions of the fuel cell system. Moreover, through the ICP-OES analysis, it was seen that the leaching of glass fibre elements was also large for the PA-based materials. Hence, it was decided at this stage that the PA-based materials will not be used for the present work. The PP-based material showcased a performance that was slightly different from the reference PPS material. It was thus carried forward and further investigated by tensile tests.

The tensile tests were carried out with three samples each at room temperature, 80 °C and 95 °C. In addition, three samples of each material, which were previously stored in the acidified product replacement water, were also tested at 95 °C. The quasi-static tensile tests were carried out using an Ibertest Testcom-50 test machine with a testing speed of 2 mm/min. For the tensile tests at 80 °C and 95 °C, a thermal climatic chamber was used. The displacements were recorded using an extensometer. Before the start of the temperature-dependent test, the chamber is kept at a set temperature for 90 min to ensure homogenous heat distribution.

The tensile testing results shown in Figure 6a clearly show that with increasing testing temperature the strength of the reference PPS material decreases considerably. The low short fibre content in the reference FRP material does not provide enough strength for the material, especially at higher temperatures. The tensile strength of around 150 MPa at room temperature falls to around 60 MPa at higher temperatures.



(**a**) (**b**)

Figure 6. Tensile test results at different temperatures (**a**) for reference PPS material, (**b**) for PP-X121 F42 material.

The tensile test for PP-X121 F42 material was conducted on probes made from 2 layers of material pressed together. Due to its higher glass fibre content along with the four layers of woven fabric, the PP-X121 F42 GMT material shows superior performances at all testing conditions in comparison with reference PPS material. At room temperature, the PP-X121 F42 was able to reach a tensile strength of around 226 MPa, and at a higher temperature of 95 °C, the loss in tensile strength was also comparatively small, as can be seen in Figure 6b. The performance of the PP-X121 F42 material in impact load cases is also superior due to the underlying material architecture, as can be seen in [35].

The major mechanical values of both materials are summarized in Tables 4 and 5. In this work, on the basis of the superior performance in the tensile tests, PP-X121 F42 FRP material was selected as the material to create the rib structure of the plastic-intensive MPP.

Table 4. E-modulus and tensile strength of reference PPS material at different temperatures.

Material Properties Reference PPS	Room Temperature	80 °C	95 °C	95 °C Immersed in Product Water
E-Modulus [GPa]	11.5	10.05	7.57	8.31
Tensile Strength [MPa]	145.4	100.7	82.4	67.2

Table 5. E-modulus and tensile strength of PP-X121 F42 material at different temperatures.

Material Properties Reference PP-X121 F42	Room Temperature	80 °C	95 °C	95 °C Immersed in Product Water
E-Modulus [GPa]	10.6	9.88	9.1	9.26
Tensile Strength [MPa]	226.6	187	147.4	122.1

3.2. Architecture of PP-X121 F42

The PPX121-F42 has a complex architecture. As shown in Figure 7, each pre-fabricated extrudate of this fibre-reinforced composite comprises two layers of endless fibres, and the remaining layers have chopped glass fibres of length 50 mm embedded in the polymer matrix, altogether resulting in a 40% weight in fibre content.

The endless glass fibres form a layer of woven fabric with an 80–20% architecture, where there are 80% of the fibres in the longitudinal direction and 20% of the fibres in the transverse direction with a biaxial plain weave. The chopped glass fibres are smeared into the polymer matrix.

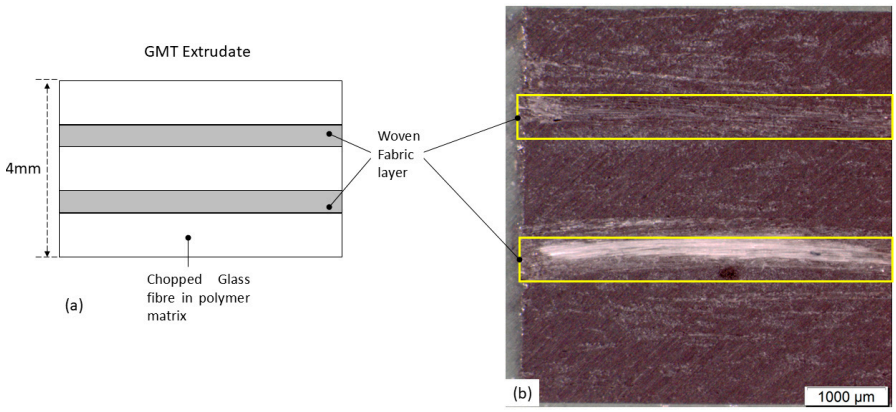


Figure 7. (**a**) PP-X121 F42 GMT schematic layup; (**b**) microscopic scan picture of PP-X121 F42 GMT.

Although the high fibre content of endless and chopped glass fibre has a positive effect on the mechanical properties of the material, it has its drawbacks in product manufacturing and development. Due to the complex architecture of woven fabrics and chopped glass fibres of length 50 mm, when using the extrudate for forming a component with rib structures, it was seen in Figure 8 that the ribs do not get entirely filled with fibres. When the extrudate is pressed into the desired rib structure through compression molding, the fibres flow only up to a certain depth of the ribs. The fibres undergo a phenomenon called the "bridging effect", where, due to the complex fibre architecture, the fibres tend not to flow the complete length of the ribs and stop halfway through the rib [35,36].

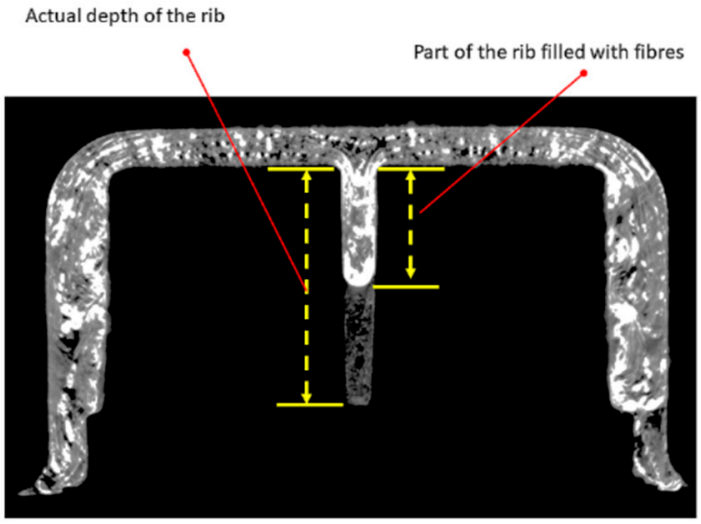


Figure 8. CT ccan of U-profile component with a middle rib [36].

Figure 8 shows a CT scan performed on a compression molded U-profile component with a vertical middle rib. The white areas show the presence of fibres, and the dark areas in the component show the regions only with polymer. This drawback of GMT material was also the reason for not choosing the PP-X103 F61 FRP material, which has an even higher percentage of fibre that hinders the flow. For product development, this fact must be kept in mind. Since the fibre filling of this kind of GMT material cannot be simulated using FEM, many detailed testing and analysis works are required for each specific part to be developed. The material properties for the FE model must be assigned manually for the deeper ribs.

3.3. Steel

For the steel plate, S355MC steel was used to obtain the necessary thickness based on the topology optimization results. Steel plate based on the final CAD design was cut to contour using water jet machining. The through holes for the fluid medium to flow through were cut in accordance with the cross-section of the holes. The steel plate will be placed and inserted into the press tool onto which the plastic GMT is pressed.

4. Fem Methodology and Target Setting

As mentioned in [11], the MPP undergoes high axial loads through the assembly of fuel cell stacks in order to reduce contact resistance and avoid any slippage of stacks under high vehicle accelerations. Prior to designing the new plastic-intensive MPP, the existing MPP needs to be benchmarked for its stiffness and rigidity to obtain the reference requirements for this work.

The geometry considered for the reference FE calculation is shown in Figure 9, which consists of the reference medium-pressure plate of aluminium with a layer of FRP mantled on the aluminium. Here, aluminium is defined as Young's modulus of 70 GPa and yield strength of 200 MPa. The reference FRP PPS material is defined as a Young's modulus of 11 GPa and yield strength of 145 MPa based on the data obtained in Section 3 on reference injection molded PPS FRP material. The MIU is not considered in the FE calculation as it is an additional component which is later screwed onto the MPP and thus does not contribute to the stiffness requirement of the system.

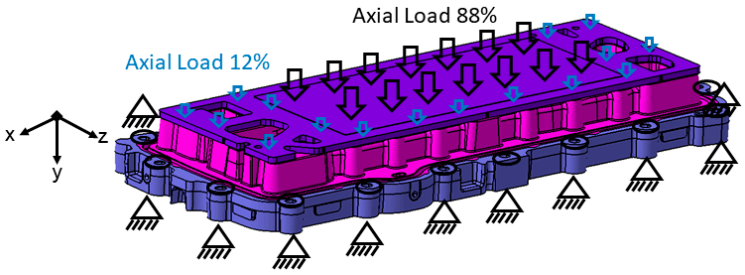


Figure 9. Load case description.

For simplification purposes, the ideal node-to-node connection is applied between the aluminium and FRP. An isotropic elastic–plastic material model was used for both aluminium and FRP layers. On top of this FRP layer is the current collector, which has frictional contact defined by the FRP layer. As depicted, the current collector transfers the axial load onto the medium-pressure plate. The load is split into two parts, whereas a major part of the load (around 88% = 53.7 kN) acts on the middle region of the current collector, where the majority of the force of bipolar cells acts. The remaining part of the load (around 12% = 7.96 kN) acts on the periphery region or on the gasket region. The load implementation was carried out based on the OEM specifications.

The components were meshed with tetrahedral elements with a mesh size of 3 mm. The medium-pressure plate is fixed in the bolt locations using RBE2 elements with the independent node fixed in all degrees of freedom. An implicit conjugate gradient solver with convergence criteria of 1e-6 was set to perform the simulation of this non-linear static load case in Optistruct by Altair. This FE methodology will later be used to evaluate the new plastic-intensive MPP.

It can be seen from Figure 10 that the highest displacement occurs in the middle region of the medium-pressure plate, where the highest axial force of the stack occurs. The stresses are highest around the bolting location in the aluminium part. For the given axial load, the stresses in the aluminium reach a maximum of 120 MPa, and the FRP reaches a maximum of 15 MPa.

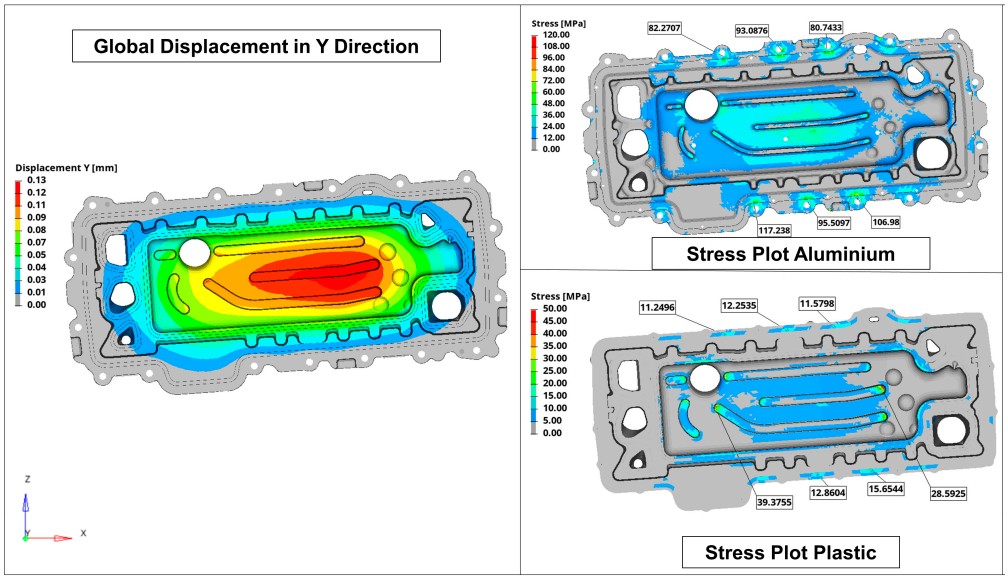


Figure 10. FEM results of reference medium-pressure plate.

5. Development of New Mpp

5.1. Topology Optimization Setup

Once the FE Calculations for the reference MPP were carried out, the design space for the topology optimization was constructed. As mentioned earlier in this work, the new plastic-intensive MPP will need to combine the functionalities of the MIU and perform the operations of MPP by guaranteeing strength requirements and holding the bipolar plates in place. Henceforth, the package space of the existing MIU is also taken into consideration for the topology optimization. Here, a steel plate of thickness of 10 mm was considered because MIU components like pumps need to be directly bolted into the steel plate with a required bolt thread depth of 8 mm in the steel plate. The rest of the design space, as shown in Figure 11, was considered to be FRP material.

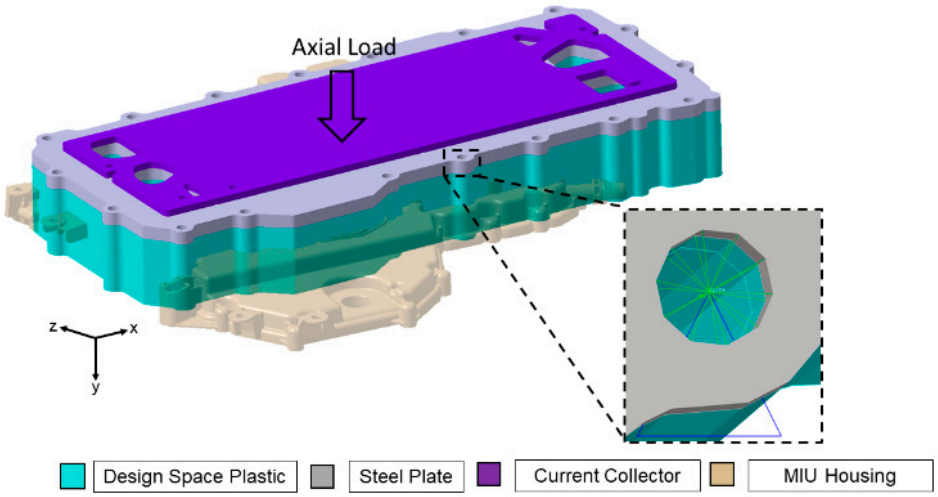


Figure 11. Design space comparison and topology boundary conditions.

For the topology optimization, an isotropic elastic material model for both steel and PP GMT was used. The Young's modulus for steel was considered to be 210 GPa with Poisson's ratio of 0.3 and a density of 7850 Kg/m^3. Since PP-X121 F42 GMT material was chosen during the material investigation in Section 3, its material properties were applied for this optimization. The average Young's modulus is 10.6 GPa, Poisson's ratio is 0.3, and the density is 1500 Kg/m^3 (see also Table 5). Here, a single material topology optimization

was set up, and all the design constraints and variables were set up for the FRP design space. As shown in Figure 11, the axial load from the current collector is applied to the steel plate through a tied contact. The FRP design space is attached to the steel plate with node-to-node equivalence. The non-design space elements here define the regions through which fluid medium flows through the fuel cell system and were hence not considered in the domain for topology optimization. RBE2 rigids were used to fix the steel at the 18 bolt locations in all degrees of freedom, similar to the load case as defined in Section 4.

As part of the design constraints, the FRP design space is set to a volume fraction of an upper bound of 0.5. This allows the optimizer to remove only a maximum of 50% of the available design space elements in the iterative process of converging to the load-compliant rib structure design. In addition to this, a compliance variable is applied to the plastic design space. As discussed in Section 1.2, the target is to minimize the compliance or to maximize the stiffness. Minimizing compliance in Equation 6 translates to reducing displacements for a given constant load. Hence, the compliance variable of the plastic design space is called into a designing objective, which sets a target of minimizing compliance with the plastic design space and achieving an even distribution of materials for the given load case. The minimization of compliance can be represented by elaborating Equation (7) as

$$\text{minimze} : \left\{ \omega_1^{\rho} \left[\frac{C(\rho) - Cmin}{Cmax - Cmin} \right]^{q} \right\}^{(1/q)} \tag{8}$$

where ω_1 is the weighting coefficient, and q is the volume fraction, weighted as 1 due to single objective optimization in our case, which is bending. For multiple load cases, the weightage will be divided based on critical criteria, having different values between 0 and 1. C(ρ) is the function of compliance to density, and Cmax is the corresponding compliance response of structure at each iteration. At each iteration, in relation to the given volume fraction and volume distribution, the overall compliance matrix of the structure is solved. Here, each iteration is converged with a particular volume distribution and a corresponding stiffness of the structure [13]. Eventually, total convergence is attained with the most optimal rib distribution and minimal displacements.

Additionally, manufacturing constraints were set to the plastic design phase, which includes a minimum thickness of member, min. dim. = 3.0 mm, a maximum thickness of member, maximum dim. = 6.0 mm, a minimum spacing between the structural members, minimum gap = 15 mm and a draw direction of y = 1. These constraints were selected based on the feasible rib design guidelines prescribed for plastic components.

5.2. Topology Optimization Results

With the boundary conditions as defined in Section 5.1, the topology optimization was carried out. The optimal rib structure needed to withstand the applied load converged after 55 iterations. Figure 12 shows the evolution of material distribution to which the solver converges over these 55 iterations. It is seen that between iterations 0 to 10, the solver first removes the complete material from the plastic design space. From iteration 10 onwards up to 40, the solver distributes material in possible ways to counteract the force by which the system is loaded. Within these iterations, the solver tends to distribute material across the steel plate. The 40th iteration shows longitudinal disjointed rib structures being formed along the Z direction. In this iteration, the rib structures have formed a clear path against the load. However, the optimization continues further as the discontinuous rib structures are not robust enough to withstand the load.

The optimization further continues until iteration 55 to reach convergence. The converged 55th iteration shows continuous stable rib geometries. It can be seen that the final rib structures, with element densities of 1, formed directly beneath the load path, with continuity and where the highest deformations occur. In certain areas, the longitudinal ribs cross paths, depicting the necessity for these ribs to be supported with ribs running across the X-direction of the design space.

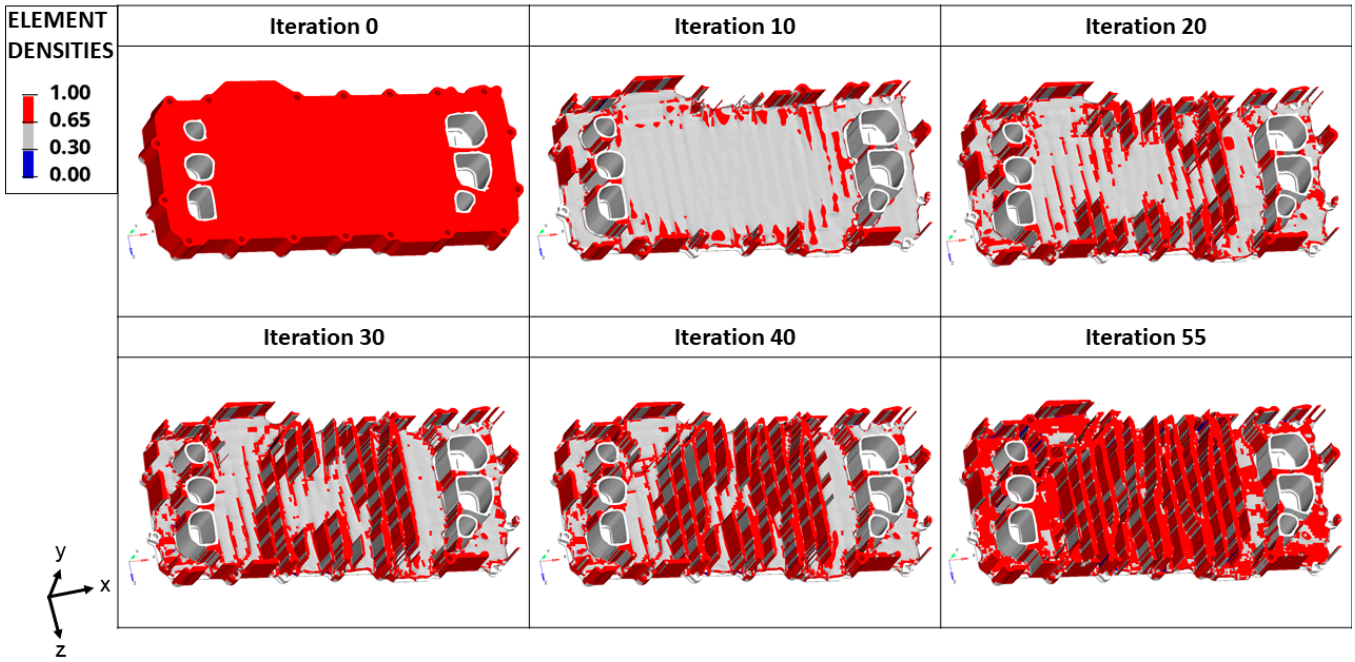


Figure 12. Topology optimization results, view from MIU side.

5.3. Conversion of Rib Geometry to Final Plastic-Intensive MPP

Once the topology optimization results were obtained, the raw rib structure was exported as an STL file and imported into the CAD environment. The obtained raw rib structure had to be utilised in the best possible way in creating the plastic-intensive MPP, whereby the functional aspects of the MPP and the MIU housing were adhered to, and manufacturing constraints were met as well. Additionally, the constraints of the material discussed in Section 3 were also taken into consideration while creating the rib structures. Figure 13 shows the results of topology optimization overlaid with the existing MIU. The obtained rib structure overlaps many existing functional features. This hinders the exact replication of the rib structure in the designing of the plastic-intensive MPP. It also shows that some of the functional features of MIU lie directly on the load path where a high concentration of rib structures was produced from the topology optimization.

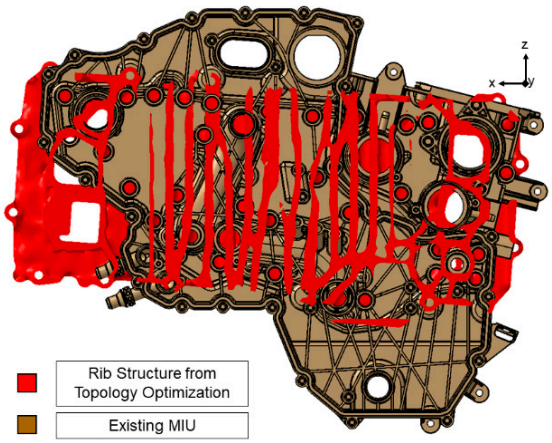


Figure 13. Comparison between topology optimization result and existing MIU housing.

5.4. Plastic-Intensive MPP—Stack Side

Upon discussion with the OEM, we found that the current collector was smaller than the old collector. The new collector, made of aluminium, will contact only the critical area of neighbouring bipolar stacks where the compressive load from the single bipolar

stacks is also high. The aluminium current collector needs to be insulated from the Steel plate, and hence, a layer of plastic with rib structures is constructed into which the current collector is embedded. This plastic layer also incorporates the cross sections of the through holes through which the various fluid materials will flow in and out of the fuel cell system. The cross sections for the fluid medium holes on the stack side were directly replicated from the existing medium-pressure plate for ease of integration with the existing fuel cell stack system.

Furthermore, the slots for the gasket around the fluid medium holes were also replicated from the existing medium-pressure plate, which will enable the reuse of existing gaskets. The plastic layer here has a base thickness of 3 mm, and the ribs have a height of 5 mm and draft angle of 1°. As shown in Figure 14, the new current collector has a 3° undercut draft angle, which enables a snug fit with the plastic.

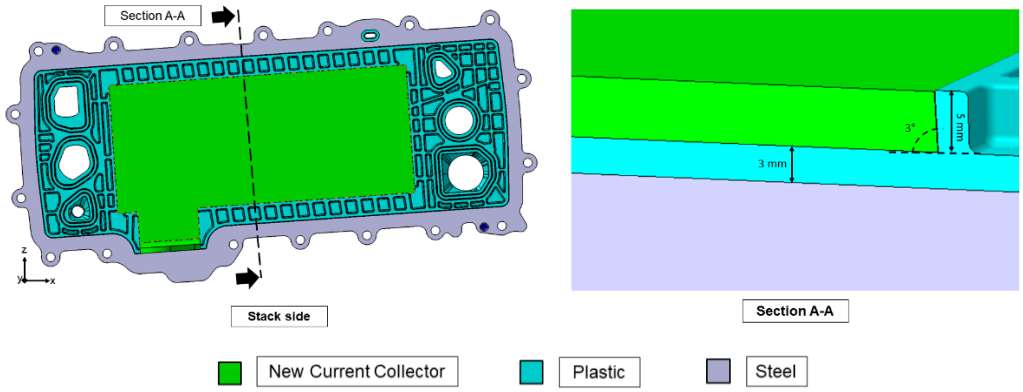


Figure 14. Newly developed MPP—Stack-side design.

5.5. Plastic-Intensive MPP—MIU Side

Figure 15 shows the rib construction of the plastic-intensive MPP on the MIU side. For this, firstly, all the bolting regions for the different pumps and cross sections of different fluid mediums were taken over directly from the existing MIU housing. Around these features the rib structures were designed. Similar to the construction on the stack side, a 3 mm layer of plastic was first constructed onto which the ribs were constructed. The rib structures were restricted to a height of 12 mm, as deeper rib structures would not be filled with fibres and rather filled only with polymer, as shown in Figure 8 [36].

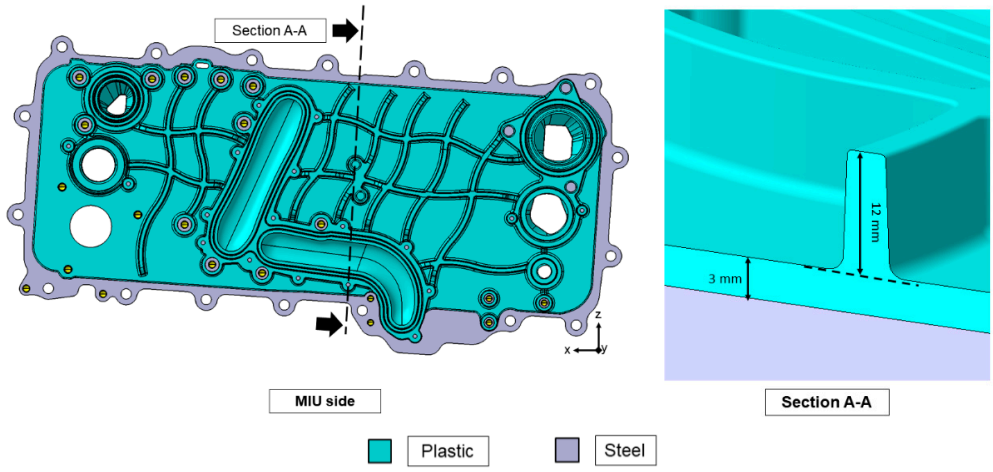


Figure 15. Newly developed MPP—MIU dide.

5.6. Plastic-Intensive MPP Concept Evaluation

Once the final CAD design of the plastic-intensive MPP was done, its stiffness was calculated through FE Simulation. The FE setup and boundary conditions defined in Chapter 16 were used to set up the FE simulation for the plastic-intensive MPP. Only the materials were replaced by the new materials, steel for the reinforcement plate and PP-X121 F42 GMT for FRP rib structures. The steel plate was defined a Young's modulus of 210 GPa and a yield strength of 360 MPa corresponding to that of S355MC grade steel. Although the PP-X121 F42 GMT is an anisotropic material, in this scope of work, the authors have represented it using an elastic–plastic material. The GMT was defined as an isotropic elastic–plastic material model with Young's modulus of 10.6 GPa and the corresponding plastic flow curve of PP-X121 F42. In the plastic-intensive MPP concept, the current collector that applies the load onto the MPP was made smaller than the existing design. Hence, the load was not split as discussed in Chapter 16, Figure 9, but rather completely applied on the middle region where bipolar plates contact the current collector.

Figure 16 shows the displacement and stresses that occur in the plastic-intensive MPP. It can be seen that the displacements in the Y direction have increased to 0.22 mm when compared to the displacements in reference MPP, which is 0.13 mm. The increase in the displacement is attributed to the fact that the complete axial load is applied on the middle region of the plastic-intensive MPP through the new current collector. The stress plot shows that the stresses in the plastic reach a maximum of 50 MPa, which is within the tensile and compressive strength of the PP-X121 F42. The highest stresses are concentrated on the ribs holding the current collector in place and near the bolting locations. The stresses in the steel plate reach a maximum of 300 MPa in the regions near the bolting locations, which is well within the yield stress of the steel material used.

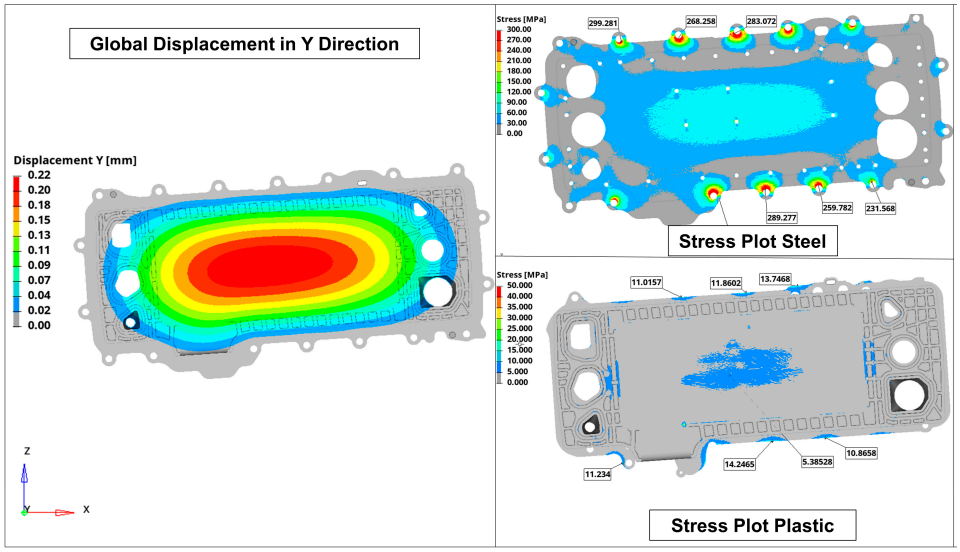


Figure 16. Newly developed MPP—FEM results.

On evaluating the plastic-intensive MPP for its package space, it has an overall height of 45% of the reference plate in the Y-direction, which is 55% less than the existing MPP and MIU housing together, as depicted in Figure 17. Comparing the weights, the plastic-intensive MPP has an 8% weight reduction compared to the existing MPP and MIU housing put together. The saved space in the new MPP can be used to assemble 50 more bipolar plates in the fuel stack, which increases the power of the fuel stack by approximately 15 kW.

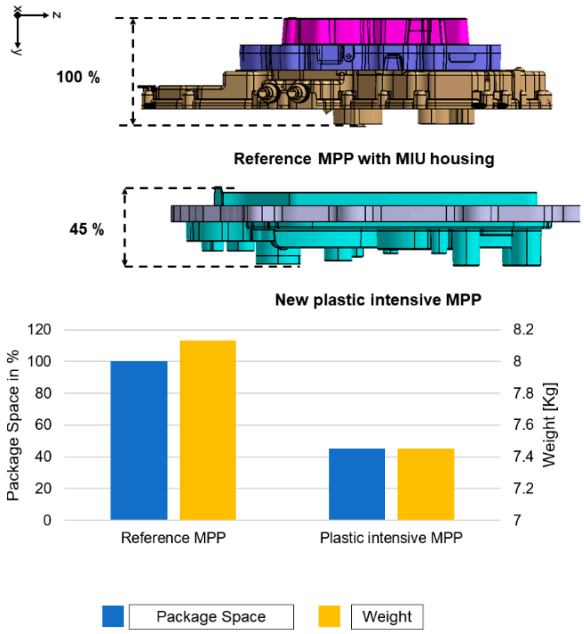


Figure 17. Package space and weight comparison between reference and new MPP.

6. Manufacturing

Once the final design was approved by the OEM, the press tool to manufacture the plastic-intensive MPP through compression molding was designed. The goal of the plastic-intensive MPP design was to achieve a high-component integrated design and manufacturing process. Figure 18 shows a schematic representation of the press tool design for the plastic MPP. It consists of an upper plate and dies for the formation of ribs on the MIU side. The MIU-side die slides into the Down holder cavity, which is connected by gas springs to the upper plate. This forms the upper half of the press tool.

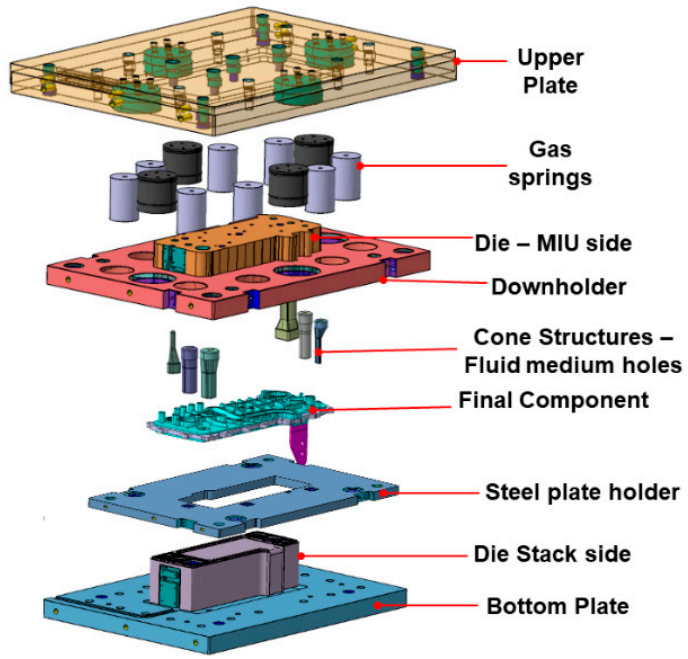


Figure 18. Press tool design for plastic-intensive MPP manufacturing.

The lower half of the press tool has a bottom plate positioned stationary on the press table, and the stack side die, which forms the rib structure on the stack side, is connected

to the bottom plate. Cone-like structures, which have the shape and cross-section of the fluid medium holes, were attached to the die correspondingly, which helped form the fluid medium holes.

The press tool, specifically the dies, which come into contact with the plastic GMT, needs to be heated to a certain temperature. For this purpose, both the MIU side and Stack side dies were heated to 80 °C using thermal heating elements placed inside the dies.

Prior to the manufacturing, the required plastic PP-X121 F42 GMT was heated in an infra-red oven to up to 190 °C. The pre-fabricated steel plate was heated to 120 °C in a separate heating plate. The pre-fabricated aluminium current collector was placed into the press tool a few minutes ahead of the actual manufacturing start, which is in contact with the stack side die. As the stack side die was heated up by the thermal heating elements, the aluminium heated up simultaneously.

Once all the components have reached their required temperatures, the manufacturing procedure, as depicted in Figure 19, starts by placing first a layer of heated GMT on top of the aluminium current collector. Then, the heated steel plate was placed and positioned on the steel plate holder. A layer of heated plastic GMT is placed on the steel plate. Finally, the press is closed, where, due to the uncompressed state of the gas springs, the downholder comes in contact with the steel plate first, compressing the gas spring and holding it in position against the steel plate holder. On further pressing, the upper die moves further down due to further compression of the gas springs. This forms the rib structures on the MIU side. Simultaneously here, the stack-side die forms the rib structures on the stack side.

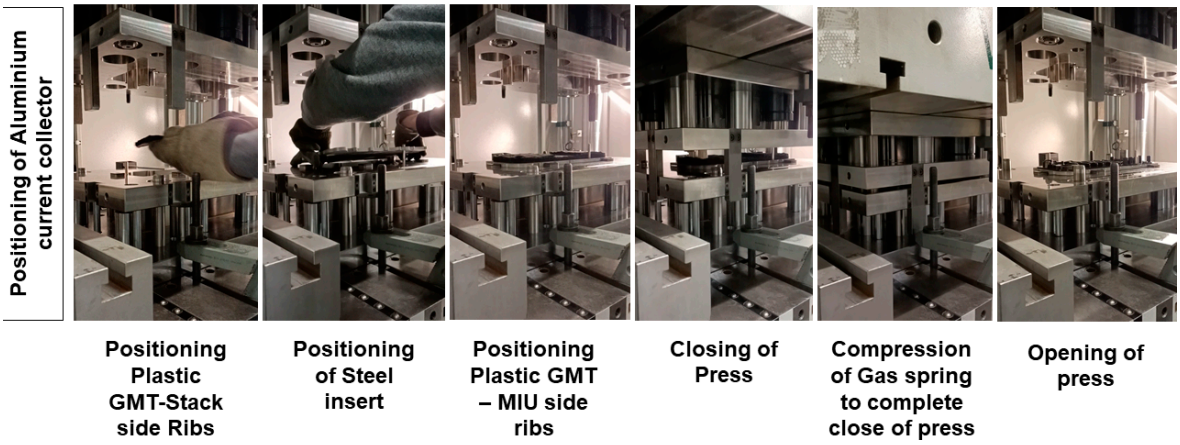


Figure 19. Process steps in compression molding of plastic-intensive MPP.

Once the press is completely closed, it is held in the closed position for up to 50 s to allow the plastic layer to solidify and cool down to reach the mold temperature. Thereafter, the mold is opened, and the final part is taken out and checked for complete filling of ribs surface quality. Based on the quality check, the temperature of the press tool dies, and the press force varies until a good quality part is produced. Figure 20 shows a final part which had a good surface finish on both the stack side and MIU side.

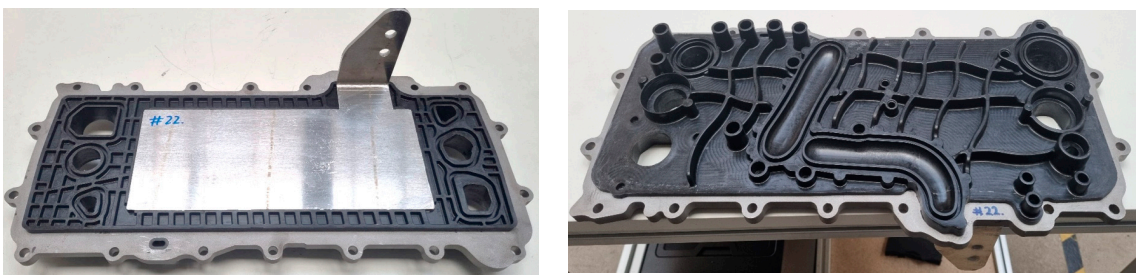


Figure 20. Plastic-intensive MPP after compression molding; stack side (**left**) and MIU side (**right**).

Once the part was taken out of the press tool, it was machined to incorporate the bolt holes into which the different pump systems would be bolted. Once the bolt holes were machined, the bolt supports and plastic inserts from the existing MPP and MIU housing were pressed into the plastic-intensive MPP. The inserts were heated and pressed to a snug fit into their corresponding position, as shown in Figure 21.

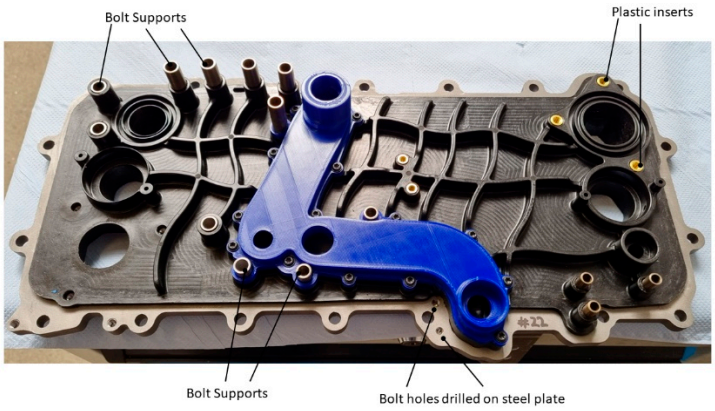


Figure 21. Plastic-intensive MPP after bolt supports and inserts were pressed.

7. Testing and Validation

The manufactured plastic MPP was then tested for its performance to verify the FE model suggested in Section 5.1. The test setup, as shown in Figure 22, consists of the plastic-intensive MPP placed on supports in the length direction at selected regions and held fest on either side in the cross direction. A dial gauge is placed directly beneath the line of the impactor, and its measuring sample is placed in contact with the plastic-intensive MPP on the MIU side.

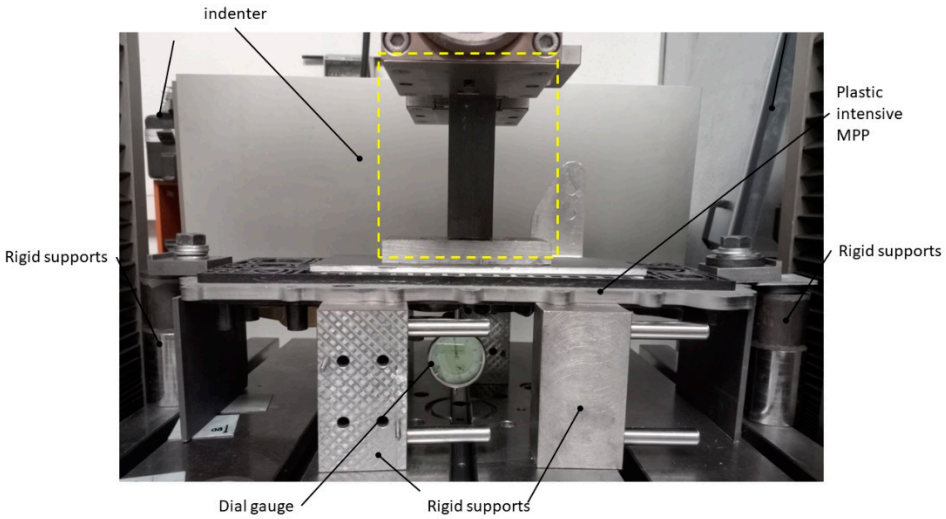


Figure 22. Test Setup for FEM verification.

Instead of a uniformly distributed load on the current collector, a rectangular indenter was used to press the MPP because it can be realized easily using a tensile test machine, as can be seen in Figure 22. The test was done using a Zwick100 tensile and compression testing machine. The displacement was measured using the dial gauge. The force was applied at 1 mm/min, and the movement of the dial gauge was recorded. On testing, the displacement reading noted on the dial gauge was 0.9 mm at the bottom-most point of measurement.

The test setup was also simulated using FEM, where the exact test setup was modelled, as shown in Figure 23a. Here, the FE model was the same as described in Sections 4 and 5.4.

However, instead of the bolting locations shown in Figure 9, the MPP was placed on supports as depicted in Figure 23a, mimicking the testing boundary conditions in Figure 22. The load was not shared amongst the nodes of the current collector as applied in the FE Model in Figure 9 and Section 5.4, but it was applied using an indenter just as in the test setup.

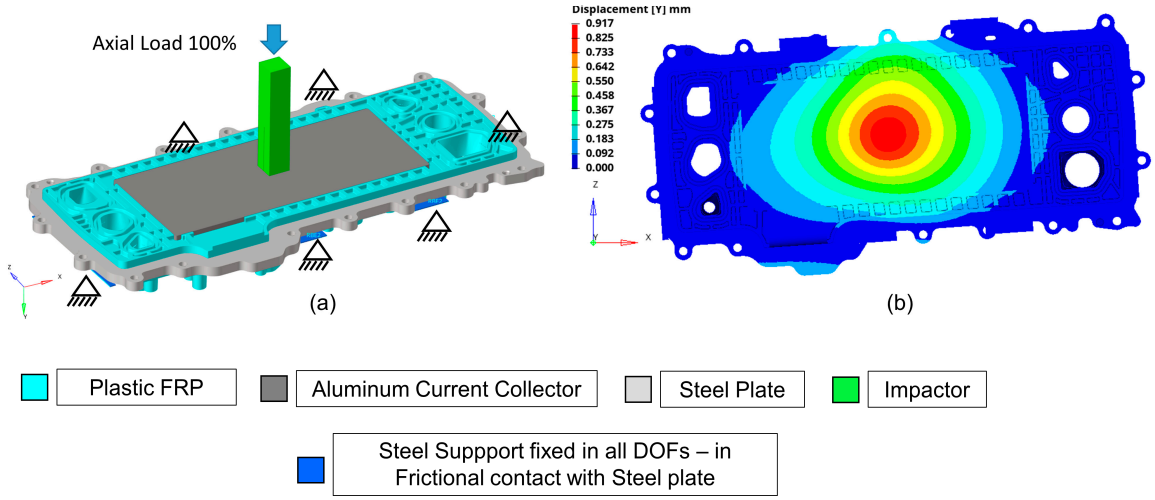


Figure 23. (**a**) Test setup in FEM simulation; (**b**) displacement plot.

The displacement calculated from the FEM simulation, as shown in Figure 23b, is 0.91 mm which produces a minimal error of 2% with the testing as compared in Table 6. The reason for the very high displacement in FEM simulation and testing is the fact that the entire axial load is concentrated through the slender indenter on a very small area of the cross-section on the current collector. Due to the good agreement between test results and FEM, the FE model used in Sections 4 and 5.4 can be considered as verified and thus also the entire development described up to now.

Table 6. Comparison of displacements in testing and simulation.

Displacement Value	In Testing	In Simulation
	0.9	0.91
% Deviation	2%	

8. Conclusion and Outlook

This work was aimed at developing a new plastic-intensive medium-pressure plate with a new manufacturing technique where weight and especially package space reduction were set as end goals. A methodology for this development was developed, which started with benchmarking the existing medium-pressure plate. Quasi-static FE analysis of the existing MPP was carried out and the displacements were determined and set as the target for the new MPP. Different FRP materials were pre-selected and analysed using mechanical and chemical testing. In close discussion with the OEM, design space and functional adaptations for the plastic-intensive MPP were fixed. Eventually, the following goals were achieved through this work.

1. PP-X142 F42 GMT material was chosen for the plastic-intensive MPP. Its mechanical properties are superior, and its chemical properties are comparable to those of the reference PPS material.
2. Using topology optimization, load-optimized rib structures for the MIU side were obtained.
3. An 8% weight reduction and a 55% package space saving were achieved through the new design, which could potentially place nearly 50 more bipolar plates and thus increase the power of the complete PEM-FC stack by 15 KW.

4. The final plastic-intensive MPP design was approved to be feasible for manufacturing: A press tool to manufacture the MPP was so designed that the pre-fabricated steel plate and aluminium current collector were placed as inserts, and the plastic rib structures were formed in accordance with the final design.
5. Manufacturing parameters which affected the final quality of the product were systematically studied within the limited number of manufactured parts.
6. The final plastic MPP design achieved a multi-component 3-in-1 design with the new current collector, medium-pressure plate and medium interface unit housing integrated into one single component. Bolting locations for the various neighbouring components were also taken into consideration.
7. The proposed FE model for MPP design was verified by tests on produced plastic-intensive MPP.

Author Contributions: Conceptualization, S.C.A., F.M. and D.H.; Methodology, S.C.A. and F.M.; Software, S.C.A.; Validation, S.C.A. and F.M.; Investigation, S.C.A., F.M., and X.F.; Writing-Original Draft Preparation, S.C.A.; Writing-Review and Editing, X.F., and S.C.A.; Supervision, X.F.; Project Administration, S.C.A.; Funding Acquisition, X.F. All authors have read and agreed to the published version of the manuscript.

Funding: This research was funded by the German Federal Ministry for Transport and Digital Infrastructure (BMVI), project name: FC-KOMP, grant number: 03B10106D.

Data Availability Statement: The necessary data for this work is contained within this article.

Acknowledgments: The authors would like to thank all partners for their support in the development of this project.

Conflicts of Interest: The authors declare no conflicts of interest.

References

1. Lamb, W.; Wiedmann, T.; Pongratz, P.; Andrew, R.; Wiedenhofer, D.; Minx, J. A review of trends and drivers of greenhouse gas emissions by sector from 1900 to 2018. *Environ. Res. Lett.* **2021**, *16*, 073005. [CrossRef]
2. Cano, Z.P.; Banham, D.; Ye, S.; Hintennach, A.; Lu, J.; Fowler, M.; Chen, Z. Batteries and fuel cells for emerging electric vehicle markets. *Nat. Energy* **2018**, *3*, 279–289. [CrossRef]
3. Gröger, O.; Hubert, A.G.; Suchsland, J.P. Review-Electromobility: Batteries or Fuel Cells? *J. Electrochem. Soc.* **2015**, *162*, 2605–2622. [CrossRef]
4. Path to Hydrogen Competitiveness. Available online: https://hydrogencouncil.com/wp-content/uploads/2020/01/Path-to-Hydrogen-Competitiveness_Full-Study-1.pdf (accessed on 14 March 2023).
5. Pundt, M.; Kirchner, M.; Stremlau, T.; Märker, G. Integrating a fuel cell system into a vehicle. *ATZ Worldw.* **2018**, *120*, 38–41. [CrossRef]
6. Pertschy, F. Das Comeback der Brennstoffzelle. Available online: https://www.automobil-produktion.de/technologie/das-comeback-der-brennstoffzelle-790.html (accessed on 20 February 2023).
7. Nakagaki, N. The Newly Developed Components for the Fuel Cell Vehicle, Mirai. *SAE Tech. Pap.* **2015**. [CrossRef]
8. Thomas, C.E. Fuel Cell and Battery Electric Vehicles Compared. *Int. J. Hydrogen Energy* **2009**, *34*, 6005–6020. [CrossRef]
9. Pollet, B.G.; Franco, A.A.; Su, H. Proton Exchange membrane Fuel cells. In *Compendium of Hydrogen Energy*; Elsevier: Amsterdam, The Netherlands, 2016; pp. 3–56.
10. Giampieri, A.; Ling-Chin, J.; Ma, Z.; Smallbone, A.; Roskilly, A.P. A review of the current automotive manufacturing practice from an energy perspective. *Appl. Energy* **2020**, *261*, 114074. [CrossRef]
11. Li, X.; Sabir, I. Review of bipolar plates in PEM fuel cells: Flow-field designs. *Int. J. Hydrogen Energy* **2005**, *30*, 359–371. [CrossRef]
12. Maheshwari, P.H.; Mathur, R.B.; Dhami, T.L. Fabrication of high strength and low weight composite bipolar plate for fuel cell applications. *J. Power Sources* **2007**, *173*, 394–403. [CrossRef]
13. Lin, P.; Zhou, P.; Wu, C.W. Multiple Objective topology optimization of end plates of proton exchange membrane fuel cell stacks. *J. Power Sources* **2011**, *196*, 1222–1228. [CrossRef]
14. Liu, B.; Wei, M.Y.; Ma, G.J.; Zhang, W. Stepwise optimization of endplate of fuel cell stack assembled by steel belts. *Int. J. Hydrogen Energy* **2016**, *41*, 2911–2918. [CrossRef]
15. Deshpande, J.; Singdeo, D.; Ghosh, P.C. Study of PEM Fuel Cell End Plate Design by Structural Analysis Based on Contact Pressure. *J. Energy* **2019**, *2019*, 3821082.
16. Youssef, M.E.; Amin, R.S.; El-Khatib, K.M. Development and performance analysis of PEMFC stack based on bipolar plates fabricated employing different designs. *Arab. J. Chem.* **2018**, *11*, 609–614. [CrossRef]

17. Syampurwadi, A.; Onggo, H.; Indriyati; Yudianti, R. Performance of PEM fuel cells stack as affected by number of cells and gas flow-rate. *IOP Conf. Ser. Earth Environ. Sci.* **2017**, *60*, 012029. [CrossRef]
18. Bharti, A.; Natarajan, R. Proton exchange membrane testing and diagnostics. In *PEM Fuel Cells. Fundamentals, Advanced Technologies and Practical Applications Book*; Elsevier: Amsterdam, The Netherlands, 2022; pp. 137–171.
19. Yan, X.; Hou, M.; Sun, L.; Liang, D.; Shen, Q.; Xu, H.; Ming, P.; Yi, B. AC Impedance characteristics of a 2 kW PEM fuel cell stack under different operating conditions and load changes. *Int. J. Hydrogen Energy* **2007**, *32*, 4358–4364. [CrossRef]
20. Fu, Y.; Hou, M.; Yan, X.; Hou, J.; Luo, X.; Shao, Z.; Yi, B. Research Progress of aluminium alloy endplates of PEMFCs. *J. Power Sources* **2007**, *166*, 435–440. [CrossRef]
21. Haider, R.; Wen, Y.; Ma, Z.F.; Wilkinson, D.P. High temperature proton exchange membrane fuel cells: Progress in advanced materials and key technologies. *R. Soc. Chem.* **2021**, *50*, 1138–1187. [CrossRef]
22. Tellez Cruz, M.M.; Escorihuela, J.; Solorza-Feria, O.; Conpan, V. Proton Exchange Membrane Fuel Cells (PEMFCs): Advances and Challenges. *Polymers* **2021**, *13*, 3064. [CrossRef]
23. Yang, D.; Tan, Y.; Li, B.; Ming, P.; Xiao, Q.; Zhang, C. A Review of the Transition Region of Membrane Electrode Assembly of Proton Exchange Membrane Fuel Cells: Design, Degradation and Mitigation. *Membranes* **2022**, *12*, 306. [CrossRef]
24. Yandrasits, M.A.; Hicks, T.M.; Pierpont, M.D. Manufacturing of Fuel Cell Membrane Electrode Assemblies Incorporating Photocurable Cationic Crosslinkable Resin Gasket. U.S. Patent No. 11/962,848, 25 June 2009.
25. Mitchell, J.; Fuller, J.T.; Gacek, T. Sulfonated PPS Fuel Cell Electrode. U.S. Patent No. 13/492,310, 12 December 2013.
26. Barbir, F. *PEM Fuel Cell, Theory and Practice*; Academic Press: Cambridge, MA, USA, 2005; pp. xiii–xv.
27. Roper, S.W.K.; Lee, H.; Huh, M.; Kim, I.Y. Simultaneous isotropic and anisotropic multi-material topology optimization for conceptual-level design of aerospace components. *Struct. Multidiscip. Optim.* **2021**, *64*, 441–456. [CrossRef]
28. Choi, W.H.; Kim, J.M.; Park, G.J. Comparison study fo some commercial structural optimization software systems. *Struct. Multidiscip. Optim.* **2016**, *54*, 685–699. [CrossRef]
29. Giele, R.; Groen, J.; Aage, N.; Andreasen, C.S.; Sigmund, O. On approaches for avoiding low-stiffness regions in variable thickness sheet and homogenizaiton-based topology optimization. *Stuructural Multidiscip. Optim.* **2021**, *64*, 39–52. [CrossRef]
30. Moritzer, E.; Heidrich, G.; Hirsch, A. Fibre Length Reduction during Injection Molding. *AIP Conf. Proc.* **2019**, *2055*, 070001.
31. Fu, S.; Lauke, B. Effects of Fiber length and fiber orientation distributions on the tensile strength of short-fiber-reinforced polymers. *Compos. Sci. Technol.* **1996**, *56*, 1179–1190. [CrossRef]
32. Fang, X.F.; Kloska, T. Hybrid forming of sheet metals with long Fiber-reinforced thermoplastics (LFT) by combined deep drawing and compression molding process. *Int. J. Mater. Form.* **2020**, *13*, 561–575. [CrossRef]
33. Tatara, R. Compression Molding. In *Applied Plastics Engineering Handbook*; William Andrew Publishing: Norwich, NY, USA, 2011; pp. 289–311.
34. Khan, R.S.; Sharma, B.; Chawla, P.A.; Bhatia, R. Inductively Coupled Plasma Optical Emission Spectrometry (ICP-OES): A Powerful Analytical Technique for Elemental Analysis. *Food Anal. Methods* **2022**, *15*, 666–688. [CrossRef]
35. Jayakumar, S.; Anand, S.; Hajdarevic, A.; Fang, X.F. Experimental and FE analyses of the crushing and bending behaviors of GMT and hybrid-formed Al-GMT structures. *Thin-Walled Struct.* **2023**, *186*, 110648. [CrossRef]
36. Kuhn, C.; Walter, I.; Taeger, O.; Osswald, T.A. Experimental and Numerical Analysis of Fiber Matrix Separation during Compression Molding of Long Fiber Reinforced Thermoplastics. *J. Compos. Sci.* **2017**, *1*, 2. [CrossRef]

Disclaimer/Publisher's Note: The statements, opinions and data contained in all publications are solely those of the individual author(s) and contributor(s) and not of MDPI and/or the editor(s). MDPI and/or the editor(s) disclaim responsibility for any injury to people or property resulting from any ideas, methods, instructions or products referred to in the content.